




Cite this: *Chem. Sci.*, 2019, 10, 10577

All publication charges for this article have been paid for by the Royal Society of Chemistry

# Well-distributed Pt-nanoparticles within confined coordination interspaces of self-sensitized porphyrin metal–organic frameworks: synergistic effect boosting highly efficient photocatalytic hydrogen evolution reaction†

Shuai Li, Hong-Min Mei, Shi-Lin Yao, Zhi-Yao Chen, Yu-Lin Lu,  Li Zhang \* and Cheng-Yong Su \*

Effective conversion of solar energy into chemical energy by visible light represents a potential strategy for sustainable development. Among which, photocatalytic hydrogen evolution reaction (HER) with a relatively small activation energy (1.23 eV, around 1000 nm light irradiation) is especially attractive. In this work, well-distributed platinum nanoparticles (Pt-NPs) with a width of about 3 nm have been successfully immobilized into the confined coordination interspaces of 3.7 nm diameter, which are facilitated by early transition metal Hf(IV)-based clusters of a self-sensitized palladium porphyrin metal–organic framework. Under visible light irradiation, the resultant Pt@Pd-PCN-222(Hf) (which is also denoted as Pt@Pd-PMOF-2(Hf)) displays superb photocatalytic activity, achieving an unprecedented maximum H<sub>2</sub> evolution rate of 22 674 μmol g<sup>−1</sup> h<sup>−1</sup> with a turn-over number (TON) of 4131.2 in 32 h and the highest turn-over frequency (TOF) of 482.5 h<sup>−1</sup> based on Pt-NPs. This photocatalyst can be recycled and reused for three successive runs without significant loss of catalytic activity. This effective strategy takes advantage of the synergetic effect between Pd-porphyrin photosensitizers and Pt-NP co-catalysts confined within nanoscale coordination interspaces incorporating hydrophilic Hf(IV)-oxo clusters.

Received 16th April 2019  
Accepted 28th September 2019

DOI: 10.1039/c9sc01866b

rsc.li/chemical-science

## Introduction

Hydrogen evolution reaction (HER) through photocatalytic water splitting is of significant importance to convert and store solar energy in the chemical bonds of H<sub>2</sub>, which is an intermediate energy carrier.<sup>1,2</sup> Although a range of photocatalysts, including molecular catalysts and inorganic semiconductors, have been developed for efficient HER,<sup>3</sup> it is yet challenging to realize recyclability and improve visible light conversion. Solar energy contains around 5% ultraviolet light, 42–43% visible light (400–700 nm) and 52–55% infrared light (>700 nm).<sup>4</sup> Metal–organic frameworks (MOFs) have emerged as a promising class of HER photocatalysts, featuring a unique capability to merge versatile photosensitizers and co-catalysts, which are able to expand the light absorption band and improve electron–

hole separation, respectively, into a single MOF as composite materials.<sup>5–8</sup>

It is convenient to engineer the coordination nanospaces of MOFs purposely for a specific functionality.<sup>9–12</sup> Excellent photosensitizers such as porphyrins could be introduced into the frameworks, giving rise to self-sensitized MOFs.<sup>13–23</sup> Porphyrins are well-known redox-active photosensitizers, as most of them have the ability to absorb visible light corresponding to the Soret and Q-bands, and display a remarkably long lifetime of the triplet excited-state. For example, the triplet state lifetimes of Rh-, Pd- and Pt-porphyrins at room temperature are typically in the order of tens to hundreds of microseconds (μs).<sup>24–26</sup> Furthermore, with the desire to improve the electron–hole separation ability, co-catalysts such as metal nanoparticles (MNPs) could be encapsulated into the coordination interspaces of MOFs. As a consequence, a Schottky barrier can form at the interface of MOFs and MNPs, and the photogenerated electrons might transfer from the LUMO of MOFs to MNPs, which could enhance electron–hole separation and then the photocatalytic performance.<sup>18,27–37</sup> Excellent catalytic performance can be achieved if MNPs were uniformly located inside the MOFs due to the synergistic catalysis between self-sensitized MOFs and incorporated MNPs. Nevertheless, the

MOE Laboratory of Bioinorganic and Synthetic Chemistry, Lehn Institute of Functional Materials, School of Chemistry, Sun Yat-Sen University, Guangzhou 510275, China. E-mail: zhli99@mail.sysu.edu.cn; cecscy@mail.sysu.edu.cn

† Electronic supplementary information (ESI) available: Details of comparison of H<sub>2</sub> evolution rates of different MOF composites, general information, physical characterization, chemical stability study, photocatalytic reactions, mechanistic study. CCDC 1920896. For ESI and crystallographic data in CIF or other electronic format see DOI: 10.1039/c9sc01866b



highest  $\text{H}_2$  evolution rates of the sole MOFs or MNPs@MOFs have not exceeded  $10\,000\ \mu\text{mol g}^{-1}\ \text{h}^{-1}$  yet.

For effective water splitting, photocatalysts should have high stability under aqueous conditions. MOFs that are constructed from highly charged metal cations (e.g.  $\text{Cr}^{3+}$ ,  $\text{Zr}^{4+}$  and  $\text{Hf}^{4+}$ ) and carboxylates are reported to have high stability in water and even acidic or basic aqueous solutions, displaying high potential for photocatalytic water splitting.<sup>38–42</sup> Early transition metals are known to be oxophilic, and thus coordination interspaces comprising early transition metal-oxo clusters and carboxylates could endow the corresponding MOFs with a hydrophilic character,<sup>43–45</sup> boosting the photocatalytic water splitting reaction. As a result, we believe that IVA group metal  $\text{Zr}^{4+}/\text{Hf}^{4+}$ -based MOFs could be effective photocatalysts towards water splitting, taking advantage of the  $\text{H}_2\text{O}$  concentration effect in confined coordination interspaces as shown in Fig. 1.

In this paper, we report the preparation of a Pd-porphyrin metal-organic framework of Pd-PCN-222(Hf) (which is also denoted as Pd-PMOF-2(Hf)) through the self-assembly of  $\text{HfCl}_4$  and PdTCPP (TCPP = tetrakis(4-carboxyphenyl)porphyrin). This MOF possessed a csq topology as in PCN-222,<sup>40</sup> MOF-545 (ref. 41) or MMPF-6,<sup>42</sup> and contained hexagonal and triangular channels with diameters of 3.7 and 1.3 nm, respectively. Pt-nanorods with consistent orientation and a width of about 3 nm were successfully immobilized into Pd-PCN-222(Hf) owing to controlled growth in the confined coordination interspaces of Pd-PCN-222(Hf). Efficient photocatalytic HER activities were achieved in the coordination nanospaces of the resultant MOF composite  $\text{Pt@Pd-PCN-222(Hf)}$ , which displayed the following features: (1) incorporating self-sensitized Pd-porphyrin with visible light absorption and a long triplet lifetime, (2) encapsulating uniformly oriented and distributed Pt-NPs as co-catalysts for effective electron-hole separation, (3) connecting hydrophilic Hf(IV)-oxo clusters with carboxylate linkers for high chemical stability and the  $\text{H}_2\text{O}$  concentration effect, and consequently, (4) achieving a synergetic effect based on the Pd-

porphyrin photosensitizer, Pt-NP co-catalyst and microenvironmental hydrophilicity. Under visible light irradiation, a maximum  $\text{H}_2$  evolution rate of  $22\,674\ \mu\text{mol g}^{-1}\ \text{h}^{-1}$  was accomplished, which was much higher than those of so far reported MOF-based HER photocatalysts (Table S1†).

## Experimental

### Synthesis of nanoscale Pd-PCN-222(Hf)

Pd(II) 5,10,15,20-tetrakis(4-carboxyphenyl)porphyrin (PdTCPP) was synthesized according to the literature.<sup>46</sup> The nanoscale Pd-PCN-222(Hf) was prepared by the reaction of PdTCPP (5 mg, 5.6  $\mu\text{mol}$ ) and  $\text{HfCl}_4$  (10 mg, 31.2  $\mu\text{mol}$ ) in DMF (3 mL) in the presence of  $\text{CF}_3\text{COOH}$  (150  $\mu\text{L}$ ) with heating at  $120\ ^\circ\text{C}$  in an oil bath. After 8 min, red needle-like crystals of Pd-PCN-222(Hf) (8.4 mg, 95% yield) were obtained, washed with DMF and ethanol several times, and dried under vacuum at  $120\ ^\circ\text{C}$  overnight. Anal. calcd for  $\text{C}_{48}\text{H}_{32}\text{PdN}_4\text{O}_{16}\text{Hf}_3 \cdot 4\text{DMF} \cdot 5\text{H}_2\text{O}$  ( $\text{C}_{60}\text{H}_{70}\text{PdN}_8\text{O}_{25}\text{Hf}_3$ ): C, 37.05; H, 3.63; and N, 5.76%. Found: C, 37.67; H, 3.44; and N, 5.25%. FT-IR (KBr)  $\nu$  3440 (br), 3133 (br), 1722 (s), 1657 (s), 1390 (s), 1273 (s), 1202 (s), 1012 (s), 798(m), and 711(m)  $\text{cm}^{-1}$ .

### Synthesis of Pt@Pd-PCN-222(Hf)

A mixture of pristine Pd-PCN-222(Hf) (20 mg) and  $\text{K}_2\text{PtCl}_4$  solution (20 mg  $\text{mL}^{-1}$ ; 100  $\mu\text{L}$ ) in DMF (4 mL) was sonicated for 15 min, and then heated at  $80\ ^\circ\text{C}$  in a drying oven. After 4 h, the product was separated as red needle-like crystals *via* centrifugation at 12 000 rpm for 3 min, washed with DMF and ethanol several times, and dried under vacuum at  $120\ ^\circ\text{C}$  overnight. FT-IR (KBr)  $\nu$  3440 (br), 3133 (br), 1722 (s), 1657 (s), 1390 (s), 1273 (s), 1202 (s), 1012 (s), 798(m), and 711(m)  $\text{cm}^{-1}$ .

### Photophysical examination

Photoluminescence spectra were recorded on an Edinburgh FLS980 Photoluminescence Spectrometer. Before the fluorescence emission test, the equivalent solid-state Pd-PCN-222(Hf) and Pt@Pd-PCN-222(Hf) samples were finely ground to avoid error. The photoluminescence lifetime experiments were performed by the time-correlated single photo counting (TCSPC) method by using a 406.5 nm picosecond pulsed diode laser, or by using the same spectrometer but with a  $\mu\text{F900}$  Xe lamp.

For ultrafast transient absorption (TA) measurements, the samples were dispersed in  $\text{CH}_3\text{CN}$  in a 0.7 mL sealed quartz cuvette, and then measurements were carried out using a femtosecond pump-probe setup consisting of Helios (Ultrafast Systems LLC) spectrometers and a regeneratively amplified Ti:sapphire laser source (Coherent Legend, 800 nm, 150 fs, 5 mJ per pulse, and 1 kHz repetition rate) in the transmission mode. A pump light of 400 nm was generated by the frequency doubling portion of the 800 nm output (75%) pulse in a  $\text{BaB}_2\text{O}_4$  (BBO) crystal, and the power intensity can be adjusted by a range of neutral-density filters, which were fixed at  $125\ \mu\text{J cm}^{-2}$  in this experiment. The delay time window between the pump and probe pulse from 0 to 7.7 ns was controlled by a motorized delay time stage.

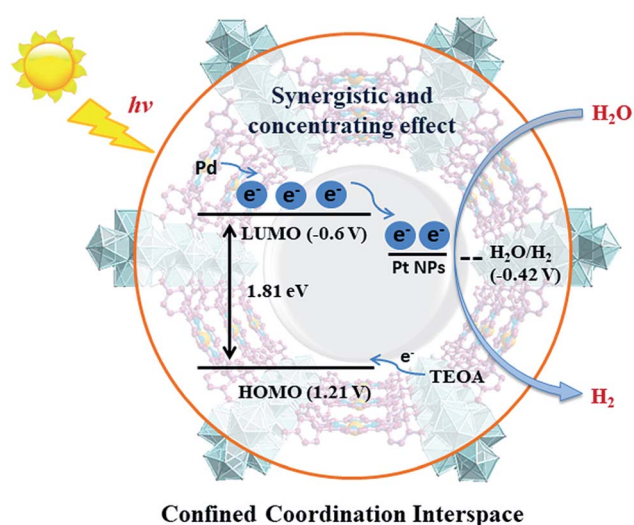


Fig. 1 Schematic illustration of the structure and photocatalytic behavior of the MOF composite  $\text{Pt@Pd-PCN-222(Hf)}$ .



## Electrochemical measurements

Electrochemical measurements were carried out using a CHI 660E electrochemical workstation (Chenhua Instrument, Shanghai, China).  $\text{Na}_2\text{SO}_4$  aqueous solution ( $0.2 \text{ mol L}^{-1}$ ) was used as the electrolyte medium. The electrochemical cell used was equipped with three electrodes, including a Pt mesh counter electrode, an Ag/AgCl reference electrode ( $3 \text{ mol L}^{-1}$  KCl) and a fluorine-doped tin oxide (FTO) glass ( $1 \times 1 \text{ cm}^2$ ) functionalized with test materials. The test materials were prepared by the following method: an activated sample (2 mg) was added to a solution of 5 wt% Nafion (10  $\mu\text{L}$ ) and ethanol (1 mL), and the resultant suspension was dispersed thoroughly *via* ultrasonication.

The photocurrent response was measured using constant voltage tracking (CVT). A 300 W Xe lamp ( $\lambda \geq 420 \text{ nm}$ ) was used as the light source, and a shutter was used to modulate the light and dark conditions during the tests. Photoresponsive signals of the samples were measured under chopped light with a bias potential of +0.13 V. The electrochemical impedance spectroscopy (EIS) measurement was performed in the frequency range from  $10^{-2}$  to  $10^5 \text{ Hz}$  with a bias potential of 2.0 V.

## Photocatalytic hydrogen evolution reaction

In a typical experiment,  $\text{Pt@Pd-PCN-222(Hf)}$  (5 mg) was suspended in a mixture of acetonitrile (10 mL), triethanolamine (2.5 mL) and deionized water (250  $\mu\text{L}$ ). The reaction mixture in a 40 mL glass vial was sonicated for 10 min, purged with nitrogen for 20 min with gentle stirring to eliminate the air, and then irradiated at room temperature with a 300 W Xe lamp equipped with a UV cut-off filter ( $\lambda \geq 420 \text{ nm}$ ). After the reaction was complete, the gaseous products were analyzed by gas chromatography (GC), which was performed using GC9790, Fuli Analytical Instrument Co., Ltd.

The catalyst was recycled and reused for three successive runs. After each run, the catalyst was separated *via* centrifugation at 12 000 rpm for 3 min and reused for the next run, which was charged with a fresh solvent, a sacrificial agent and water.

## Results and discussion

### Synthesis, structure and stability

$\text{Pd-PCN-222(Hf)}$  with up to 95% yield was prepared by the reaction of PdTCPP and  $\text{HfCl}_4$  in the presence of  $\text{CF}_3\text{CO}_2\text{H}$  as a modulating reagent after being heated at  $120^\circ\text{C}$  in an oil bath for 8 min (Fig. 2). The bulk purity was confirmed by powder X-ray diffraction (PXRD) patterns (Fig. 3a), which fit well with the simulated patterns of PCN-222(Hf) constructed with metal free porphyrin ligand TCPP. The coordination framework of  $\text{Pd-PCN-222(Hf)}$  comprises  $\text{Hf}_6(\text{OH})_8$  clusters linked by Pd-porphyrin ligands, giving rise to hexagonal mesochannels with a diameter of 3.7 nm as well as trigonal microchannels with a diameter of 1.3 nm.<sup>40</sup> The square planar geometry of Pd(II)-porphyrin was clearly shown by X-ray single crystallography of PdTMCPP (TMCPP = 5,10,15,20-tetrakis(4-methoxycarbonylphenyl)porphyrin) (Fig. S1†). Scanning electron microscopy (SEM) and transmission electron microscopy (TEM) measurements disclosed that the as-prepared  $\text{Pd-PCN-222(Hf)}$  samples are of nanorod shape with about 300 nm width and 500 nm length (Fig. 4a and b).

The MOF composite  $\text{Pt@Pd-PCN-222(Hf)}$  was prepared by the *in situ* formation of Pt NPs in the coordination interspaces of the hexagonal mesochannels (3.7 nm) in  $\text{Pd-PCN-222(Hf)}$ , which was accomplished by the solvothermal reaction of  $\text{Pd-PCN-222(Hf)}$  and  $\text{K}_2\text{PtCl}_4$  in DMF at  $80^\circ\text{C}$  for 4 h (Fig. 2). The presence of both Pd and Pt was confirmed by the X-ray photoelectron spectroscopy (XPS) examination (Fig. S2†). The metallic Pd(0) and Pt(0) species were clearly identified by the binding energies at 338.09 and 343.34 eV assignable to the  $3d_{5/2}$  and  $3d_{3/2}$  levels of Pd(0), respectively, as well as the binding energies at 71.14 and 74.47 eV related to the  $4f_{7/2}$  and  $4f_{5/2}$  levels of Pt(0), respectively (Fig. S2b and c†).<sup>47,48</sup> The weight loading of Pt-NPs was determined to be 0.92% using an inductively coupled plasma optical emission spectrometer (ICP-OES). The PXRD patterns of  $\text{Pt@Pd-PCN-222(Hf)}$  closely matched with those of  $\text{Pd-PCN-222(Hf)}$ ,

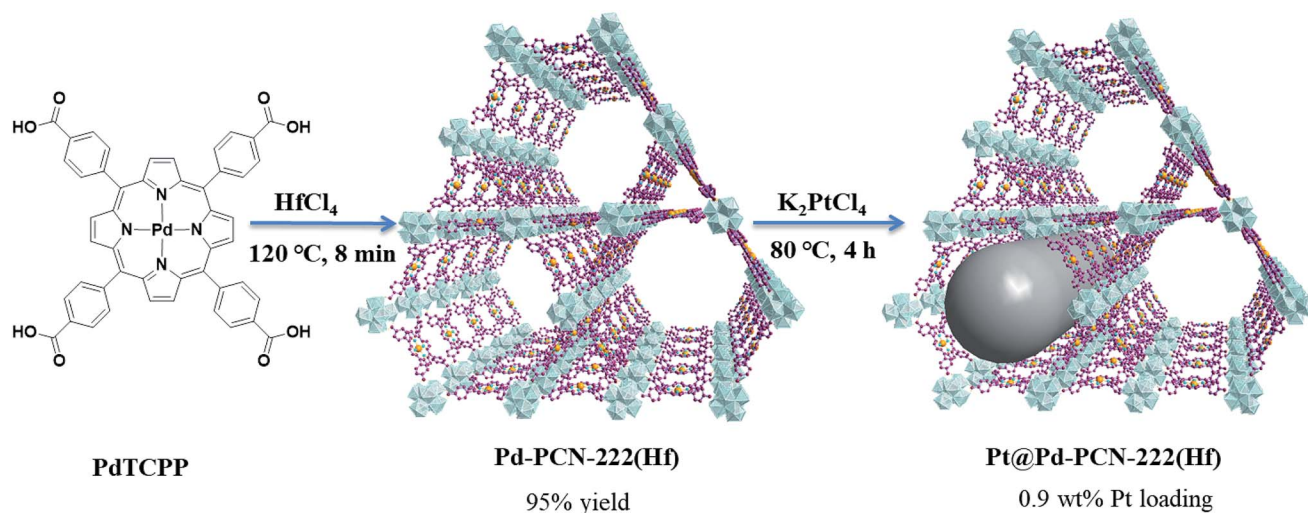


Fig. 2 The syntheses of  $\text{Pd-PCN-222(Hf)}$  and  $\text{Pt@Pd-PCN-222(Hf)}$ .



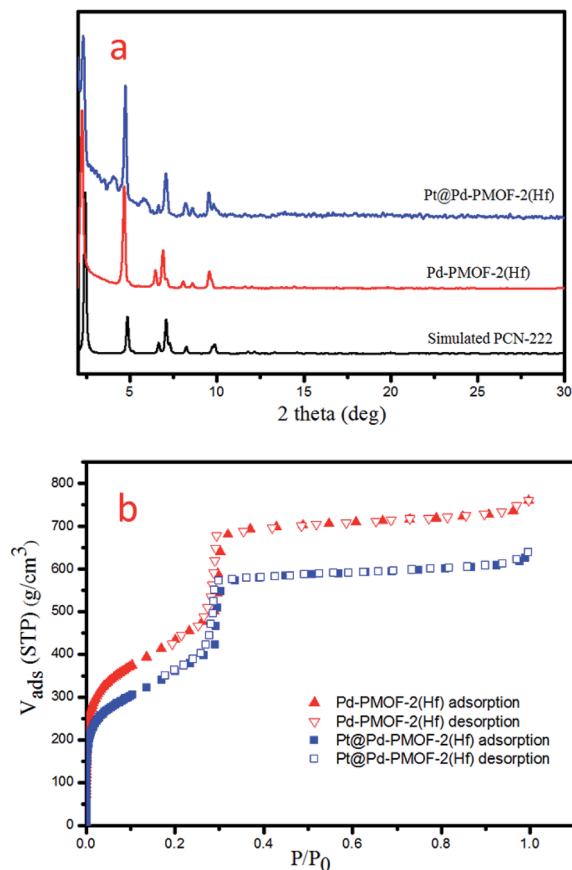


Fig. 3 PXRD patterns (a) and  $N_2$  sorption isotherms at 77 K (b) of Pd-PCN-222(Hf) and Pt@Pd-PCN-222(Hf).

indicating that the framework and crystallinity of Pd-PCN-222(Hf) remain well after introduction of Pt-NPs (Fig. 3a).

The  $N_2$  uptakes of Pd-PCN-222(Hf) and Pt@Pd-PCN-222(Hf) at 77 K were 760 and 640  $\text{cm}^3 \cdot \text{g}^{-1}$  (STP), respectively, and the Brunauer-Emmett-Teller (BET) surface areas were calculated to be 1511 and 1263  $\text{m}^2 \cdot \text{g}^{-1}$ , respectively. This showed a slight decrease upon the loading of Pt-NPs into the pores of Pd-PCN-222(Hf) (Fig. 3b). The activated samples of Pd-PCN-222(Hf) and Pt@Pd-PCN-222(Hf) exhibited remarkable water adsorption capacities with uptakes of 881 and 1035  $\text{cm}^3 \cdot \text{g}^{-1}$ , respectively, at 298 K and  $P/P_0 = 0.85$  (Fig. S3†). The water uptake ability of Pt@Pd-PCN-222(Hf) was even higher than that of the primitive Pd-PCN-222(Hf). Significant hysteresis loops between the adsorption-desorption curves were observed, indicative of physical interactions between the adsorbed water molecules and the hydrophilic Hf(IV)-oxo clusters.<sup>43–45</sup> Although the inner coordination interspaces contain hydrophilic Hf(IV)-oxo clusters, the overall porous Pd-PCN-222(Hf) displayed some kind of water resistance at a relatively low pressure, and water uptake abruptly occurred at  $P/P_0 \approx 0.6$ . The hysteresis behaviors also suggested that desorption of water molecules was lagging. This implied that the porous Pd-PCN-222(Hf) was able to prevent catalytic sites inside the coordination interspaces from immediate exposure to enormous water molecules, which might cause deterioration of catalysts and hamper the HER process. In

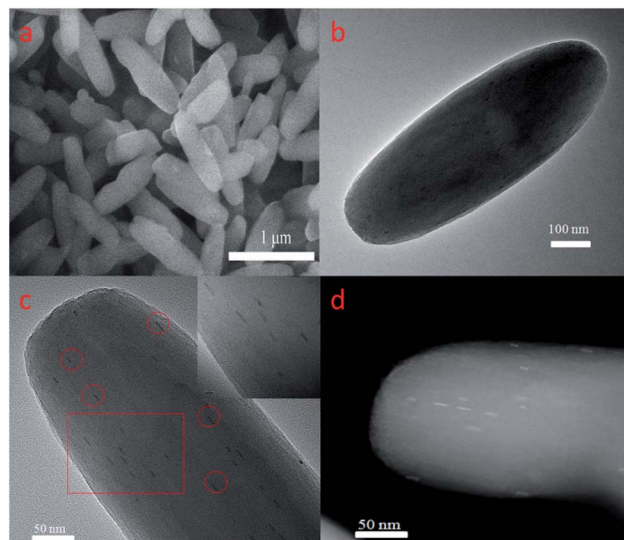


Fig. 4 SEM (a) and TEM (b) images of Pd-PCN-222(Hf), and median-magnification TEM (c), high-magnification TEM (insert c) and aberration-corrected HAADF-STEM (d) images of Pt@Pd-PCN-222(Hf).

comparison, the adsorbed water molecules were transiently concentrated inside the coordination interspaces for photocatalysis rather than freely releasing from Pt@Pd-PCN-222(Hf).

The presence of Pt-NPs in Pt@Pd-PCN-222(Hf) was clearly observable in TEM images, as marked with the red circles in Fig. 4c and the inset, and more discernible as bright spots in the high-angle annular dark-field scanning TEM (HAADF-STEM) tomogram (Fig. 4d). The Pt-NPs with a width of around 3 nm and a length range of 7–15 nm (Fig. S4†) displayed consistent orientation, suggesting a confined growth of Pt-NPs in the coordination interspaces of the hexagonal mesochannels (3.7 nm) in Pd-PCN-222(Hf). The internal Pt-NP location was further demonstrated by the electron tomographic reconstruction of Pt@Pd-PCN-222(Hf) shown in Fig. S5.†

In comparison, the majority of the reported Pt-NPs@MOF materials displayed several issues: (1) the morphology of Pt-NPs was unclear due to the lack of related characterization; (2) the Pt-NPs were deposited on the external surfaces of MOFs; (3) the agglomeration of Pt-NPs occurred; (4) the sizes of Pt-NPs were larger than those of MOF inner cavities, indicative of the distortion/degradation of MOFs during the formation of Pt-NPs; or (5) the Pt-NPs weren't dispersed uniformly in the pores of MOFs.<sup>49,50</sup>

Both Pd-PCN-222(Hf) and Pt@Pd-PCN-222(Hf) exhibited excellent chemical stability. The fresh samples were soaked in various organic solvents, including methanol, acetonitrile, acetone, dichloromethane, ethyl acetate and water for seven days, and then the PXRD patterns of the recycled samples were checked, which suggested that the crystallinity of the samples was well retained after these treatments (Fig. S6 and S7†). Furthermore, both Pd-PCN-222(Hf) and Pt@Pd-PCN-222(Hf) were stable after being immersed in aqueous solutions of a wide pH range from 1 to 12 for 24 h (Fig. S8 and S9†).



## Photocatalytic activities

Prior to the photocatalytic study, the light absorption range and the LUMO potential of Pd-PCN-222(Hf) and Pt@Pd-PCN-222(Hf) were examined. Solid UV-vis absorption spectroscopy showed that both Pd-PCN-222(Hf) and Pt@Pd-PCN-222(Hf) possessed strong light absorption extending to around 700 nm with two main peaks, which were the Soret band ( $\sim 415$  nm) and Q band ( $\sim 523$  nm) (Fig. S10<sup>†</sup>). The Mott-Schottky (M-S) plots were measured at frequencies of 500, 1000 and 1500 Hz (Fig. S11–S13<sup>†</sup>). The positive slopes of the M-S plots were characteristic of n-type semiconductors. The flat band positions determined from the intersections were approximately  $-0.6$  V (vs. NHE) for PdTMCPP, Pd-PCN-222(Hf) and Pt@Pd-PCN-222(Hf). It was generally accepted that the flat band was equal to the conduction band (LUMO) for an n-type semiconductor, which suggested that the LUMO positions of PdTMCPP, Pd-PCN-222(Hf), and Pt@Pd-PCN-222(Hf) were also approximately  $-0.6$  V (vs. NHE). Based on Tauc plots, the band gap energies ( $E_g$ ) of PdTMCPP, Pd-PCN-222(Hf), and Pt@Pd-PCN-222(Hf) were calculated to be 1.81, 2.13 and 2.14 eV, respectively. Therefore, the valence bands (HOMO) were accordingly obtained (Fig. S14–S16<sup>†</sup>). Given the more negative LUMO potentials in comparison to the proton reduction ( $-0.42$  V vs. NHE, pH = 7), it was thermodynamically feasible for the Pd-porphyrin MOF-based materials to behave as HER photocatalysts.

Encouraged by high chemical stability, strong visible light absorptivity and appropriate LUMO potentials, the photocatalytic HER for water splitting was carried out. The hydrogen evolution experiments were firstly conducted using triethanolamine (TEOA) as a sacrificial agent in different aqueous-organic solvents, including *N,N*-dimethylformamide (DMF), dimethylacetamide (DMAC), pyrrole, dimethyl sulfoxide (DMSO), acetone, isopropanol (*i*PrOH), and acetonitrile ( $\text{CH}_3\text{CN}$ ), under visible light irradiation ( $\lambda \geq 420$  nm) (Table S2,† entries 1–7). Catalytic results disclosed that a  $\text{H}_2$  evolution rate up to  $22\,674\ \mu\text{mol g}^{-1}\text{ h}^{-1}$  after irradiation for 3 h was achieved in  $\text{CH}_3\text{CN}$ , which was around twice that in *i*PrOH, DMF, acetone and DMAC. For comparison, the  $\text{H}_2$  evolution rates in DMSO and pyrrole were 2470 and  $117\ \mu\text{mol g}^{-1}\text{ h}^{-1}$ , respectively, which were rather lower. In addition to TEOA, other sacrificial agents such as methanol ( $\text{CH}_3\text{OH}$ ), *N,N*-dimethylaniline (DMA), ascorbic acid and 1,3-dimethyl-2-phenyl-2H-benzimidazole (BIH) were also screened, unveiling that TEOA was the best sacrificial agent in this system (Table S2,† entries 1, 8–11). The optimal amounts of TEOA and water were explored, and the results are shown in entries 1 and 12–15.

Under the optimal reaction conditions, the catalyst durability test of Pt@Pd-PCN-222(Hf) was performed and the  $\text{H}_2$  evolution rate was monitored every 1 h (Fig. 5). The  $\text{H}_2$  evolution rate increased from the initial  $18\,920\ \mu\text{mol g}^{-1}\text{ h}^{-1}$  after irradiation for 1 h to a maximum  $22\,674\ \mu\text{mol g}^{-1}\text{ h}^{-1}$  after 3 h, and then gradually decreased to  $14\,510\ \mu\text{mol g}^{-1}\text{ h}^{-1}$  after 8 h. After irradiation for 32 h, the  $\text{H}_2$  evolution amount arrived at an equilibrium of  $194\,168\ \mu\text{mol g}^{-1}$ , while the corresponding rate dropped to  $6068\ \mu\text{mol g}^{-1}\text{ h}^{-1}$  (Table S3<sup>†</sup>). Based on the loaded Pt-NPs, the initial TON and TOF were calculated to be 1447.3

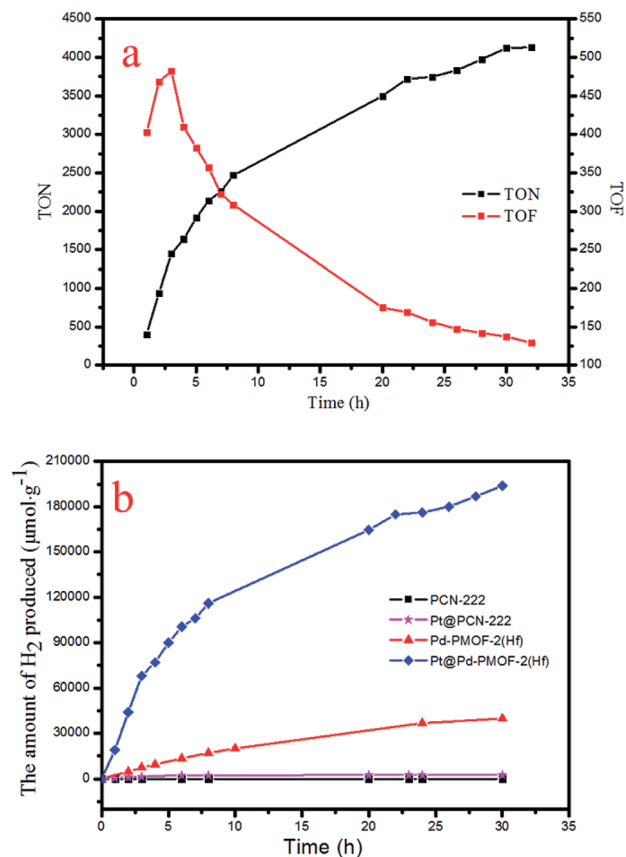


Fig. 5 Accumulated TONs ( $\text{TON} = n(\text{H}_2)/n(\text{Pt})$ ) and TOFs ( $\text{TOF} = d(\text{TON})/dt$ ) based on Pt-NPs in the catalyst durability test of Pt@Pd-PCN-222(Hf) over 32 h (a), and the amount of  $\text{H}_2$  ( $\mu\text{mol g}^{-1}$ ) produced by different photocatalysts (b).

and  $482.5\ \text{h}^{-1}$  for 3 h photoreaction, respectively. After 32 h, the accumulated TON reached 4131.2 while the TOF decreased to  $129.1\ \text{h}^{-1}$  without replenishing the sacrificial agent. This suggested that Pt@Pd-PCN-222(Hf) had excellent catalytic durability. For further proof, Pt@Pd-PCN-222(Hf) can be recycled and reused for three successive runs. The recycled Pt@Pd-PCN-222(Hf) did not show a significant loss of catalytic activity (Fig. 6), indicating that the HER photocatalytic ability of Pt@Pd-PCN-222(Hf) was well recovered when reused under fresh solvent, sacrificial agent and water conditions. As shown in the TEM image, no obvious morphology change occurred after the first run (Fig. S17<sup>†</sup>). PXRD and XPS examination of the recycled samples of Pt@Pd-PCN-222(Hf) verified that its main composition and crystallinity remained intact and the valences of Pd(2+) and Pt(0) did not change after the catalytic reactions (Fig. S18 and S19<sup>†</sup>). ICP-OES analysis of the filtrate after catalysis indicated that the amount of Pd leaching into the reaction mixture was around 3.5%.

The photocatalytic HER performances of PCN-222(Hf), Pd-PCN-222(Hf) and Pt@PCN-222(Hf) were compared (Fig. 5b and Table S4<sup>†</sup>). It was reported that, for MOFs constructed from Zr-O clusters and organic linkers with  $\pi$  conjugation, the ligands could behave as light harvesters. After the ligands were photo-excited, the photogenerated electrons transferred to Zr-oxo



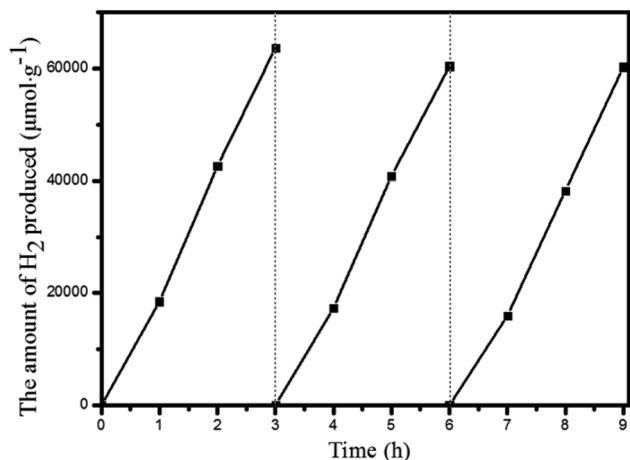


Fig. 6 Recycling experiments of Pt@Pd-PCN-222(Hf).

clusters *via* linker-to-cluster charge transfer (LCCT). Zr(IV) ions were then reduced to Zr(III), which promoted the subsequent photoreduction reaction.<sup>51</sup> Nonetheless, the Hf-based PCN-222(Hf) did not show any activity of photocatalytic HER. After the loading of Pt-NPs as a co-catalyst, a catalytic rate of  $441 \mu\text{mol g}^{-1} \text{h}^{-1}$  was detected. For comparison, Pd-PCN-222(Hf) that was isostructural with PCN-222(Hf) but had a Pd metal in the porphyrin center exhibited a higher photocatalytic efficiency ( $2476 \mu\text{mol g}^{-1} \text{h}^{-1}$ ), indicating that Pd-porphyrin itself played a critical role in the photocatalytic reaction. Furthermore, after the loading of Pt-NPs as a co-catalyst, a much higher  $\text{H}_2$  production rate ( $22\,674 \mu\text{mol g}^{-1} \text{h}^{-1}$ ) of Pt@Pd-PCN-222(Hf) was accomplished, which was about 51 and 10 times higher than those of Pt@PCN-222(Hf) and Pd-PCN-222(Hf), respectively.

The catalytic performance of Pt@Pd-PCN-222(Hf) was also compared with those of known Pt@MOF (or Pt/MOF) composites under visible light irradiation (Table S1†). Pt-NPs were deposited in a range of stable MOFs, such as MIL-100(Fe), UiO-66-NH<sub>2</sub>(Zr), and MIL-125-NH<sub>2</sub>(Ti), which gave  $\text{H}_2$  evolution rates of 98, 257 and  $367 \mu\text{mol g}^{-1} \text{h}^{-1}$ , respectively.<sup>27–29</sup> Taking advantage of the strong absorption of visible light by porphyrin compounds, porphyrin-based MOFs loaded with Pt-NPs were reported to offer a  $\text{H}_2$  evolution rate up to  $341 \mu\text{mol g}^{-1}$

$\text{h}^{-1}$ .<sup>18,31,32</sup> Dye-sensitization became a relatively mature technology for visible-light harvesting, which was employed to enhance the catalytic efficiency of Pt@UiO-66 ( $116 \mu\text{mol g}^{-1} \text{h}^{-1}$ ) and Pt/NH<sub>2</sub>-MIL-101 ( $477 \mu\text{mol g}^{-1} \text{h}^{-1}$ ).<sup>33,34</sup> Ternary MOF composites of Pt@MIL-125/Au and Pt@MIL-101/CdS with additional plasmonic Au-NP and CdS semiconductors, respectively, were also prepared and examined in photocatalytic HER, and the  $\text{H}_2$  evolution rates increased from a hundred scale to a thousand range up to  $7550 \mu\text{mol g}^{-1} \text{h}^{-1}$ .<sup>35,36</sup> In short, Pt@Pd-PCN-222(Hf) represented an exceptionally efficient HER photocatalyst among MOF composites in terms of the  $\text{H}_2$  evolution rate and catalytic durability.

## Reaction mechanism

For a better understanding of the reaction mechanism, the electron-hole separation efficiency was firstly studied *via* ultrafast transient absorption (TA) spectroscopy.<sup>52–55</sup> In the TA measurements, a pump-probe configuration with a femto-second visible pump and a white-light continuum probe was adopted. The center wavelength of the pump pulses was chosen to be 400 nm, which could effectively excite porphyrin MOFs. The TA of Pd-PCN-222(Hf) and Pt@Pd-PCN-222(Hf) both featured a broad excited-state absorption (ESA) around 505 nm accompanied by a ground-state bleaching (GSB) centered around 450 nm, which displayed positive and negative absorbance changes ( $\Delta A$ ), respectively (Fig. 7a and b). The recovery around 505 nm was characterized by two time constants, that is,  $\tau_1 = 17\,500 \text{ ps}$  (76.7%) and  $\tau_2 = 11.4 \text{ ps}$  (23.3%) for Pd-PCN-222(Hf), and  $\tau_1 = 2.19 \text{ ps}$  (16.6%) and  $\tau_2 = 7260 \text{ ps}$  (83.4%) for Pt@Pd-PCN-222(Hf) (Fig. 7c and Table S5†). For comparison, Pt@Pd-PCN-222(Hf) exhibited an acceleration of the TA kinetics compared to Pd-PCN-222(Hf). Within the probe-delay limit of our pump/probe spectrometer ( $\sim 7.7 \text{ ns}$ ), the  $\Delta A$  recovery converged to an asymptote with a non-zero, indicative of an extra extremely long lifetime.

Next, steady-state photoluminescence (PL) spectroscopy was carried out to characterize the photophysical behaviors of Pd-PCN-222(Hf) and Pt@Pd-PCN-222(Hf) (Fig. S20†). Upon excitation ( $\lambda_{\text{ex}} = 422 \text{ nm}$ ), they both displayed two main PL peaks around 654 and 722 nm. The emission intensity of Pt@Pd-PCN-222(Hf) was remarkably reduced in comparison to that of Pd-

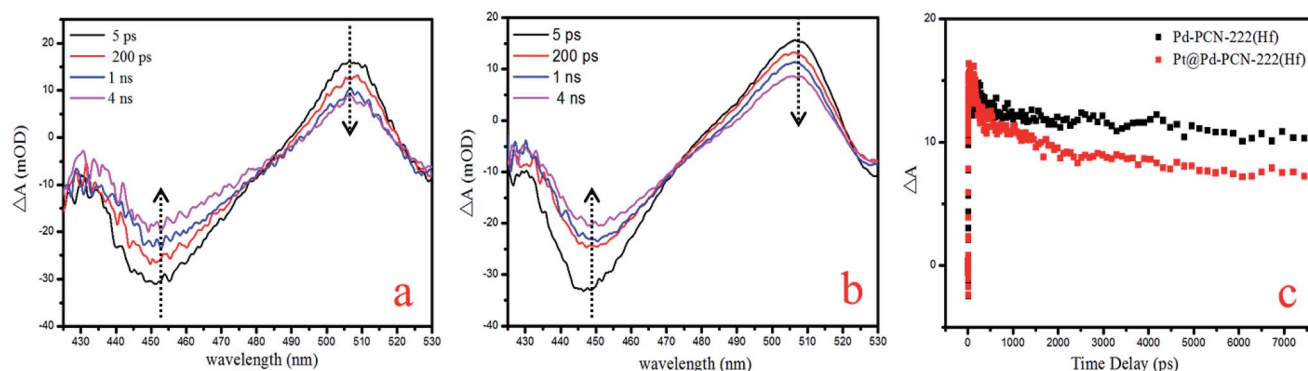


Fig. 7 TA spectra of Pd-PCN-222(Hf) (a) and Pt@Pd-PCN-222(Hf) (b), and TA kinetics at the probing wavelength of 505 nm (c).





PCN-222(Hf), suggesting that the recombination rate of photo-generated electron-hole pairs was decreased after the Pt-NPs were introduced into the coordination interspaces of Pd-PCN-222(Hf), due to the formation of a Schottky barrier at the interface of Pd-PCN-222(Hf) and Pt-NPs. The PL lifetimes of PCN-222, Pd-PCN-222(Hf) and Pt@Pd-PCN-222(Hf) were then examined, which were calculated to be 1.2 ns, 113.4  $\mu$ s and 91.6  $\mu$ s, respectively, at 298 K under vacuum (Fig. S21 and Table S6†). Such significantly long-lived triplet states in Pd-PCN-222(Hf) and Pt@Pd-PCN-222(Hf) were competent for electron transfer, leading to subsequent photoreactions. According to the iterative extended Hückel (IEH) model, the strong phosphorescence of  $d^8$  Pd(II) porphyrins should be due to the mixing of empty  $e_g$  ( $\pi^*$ ) of porphyrin and the filled  $d_{\pi}$  of the metal, which was also called  $\pi$ -back bonding, giving rise to a large spin-orbit coupling, rapid intersystem crossing and high triplet yields.<sup>56</sup>

Finally, the photocurrent response and electrochemical impedance spectroscopy (EIS) measurements were performed to unveil the charge-separation efficiency. Pt@Pd-PCN-222(Hf) possessed the strongest photocurrent response among all samples, indicating that the recombination of photogenerated electrons and holes was largely inhibited and effective charge

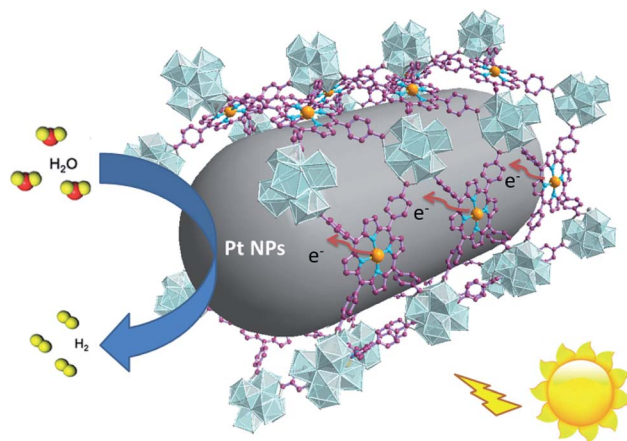


Fig. 9 The possible HER reaction mechanism of Pt@Pd-PCN-222(Hf).

transfer occurred from Pd-PCN-222(Hf) to Pt-NPs under visible-light irradiation (Fig. 8a). This argument was also supported by EIS results (Fig. 8b), where Pt@Pd-PCN-222(Hf) exhibited the smallest radius, indicative of its fastest interfacial charge transfer.

According to photocatalytic results and physical characterization, a possible mechanism was proposed (Fig. 1 and 9): the Pd-porphyrin was excited by visible light, giving rise to the excited-states. And then, the electrons transferred from the LUMO of the Pd-porphyrin ligand to Pt-NPs, where the  $H_2O$  molecules were reduced to generate  $H_2$ . Nevertheless, the LCCT mechanism, in which the photogenerated electrons firstly transferred to the Hf-O clusters, and then flowed to Pt-NPs, could not be ruled out.

The remarkable  $H_2$  evolution activity of Pt@Pd-PCN-222(Hf) might be ascribed to three factors. Firstly, the Pd-porphyrin photosensitizers featuring long-lived room temperature phosphorescence were spatially arranged in Pd-PCN-222(Hf), assisting a wide range of visible light absorption without mutual electron coupling quenching. Secondly, the Pt-NPs were well oriented and distributed into the confined coordination interspaces of Pd-PCN-222(Hf) to form a Schottky barrier on the interface with Pd-porphyrin photosensitizers, accelerating the charge transfer and electron-hole separation. Thirdly, the Hf(IV)-based MOF provided hydrophilic Hf(IV)-oxo clusters with  $H_2O$  accumulation for photocatalytic water splitting. In short, these collaborative effects inside the functional coordination interspaces of Pd-PCN-222(Hf) boosted highly efficient photocatalytic HER.

## Conclusion

Photocatalytic water splitting for  $H_2$  evolution is vital to energy and environmental science. In this work, we demonstrate a strategy for the design of a powerful HER photocatalyst by taking advantage of the synergistic effect among the Pd-porphyrin photosensitizer with long-lived room temperature phosphorescence, Pt-NPs as co-catalysts that grew in the confined coordination interspaces of Pd-PCN-222(Hf), and the

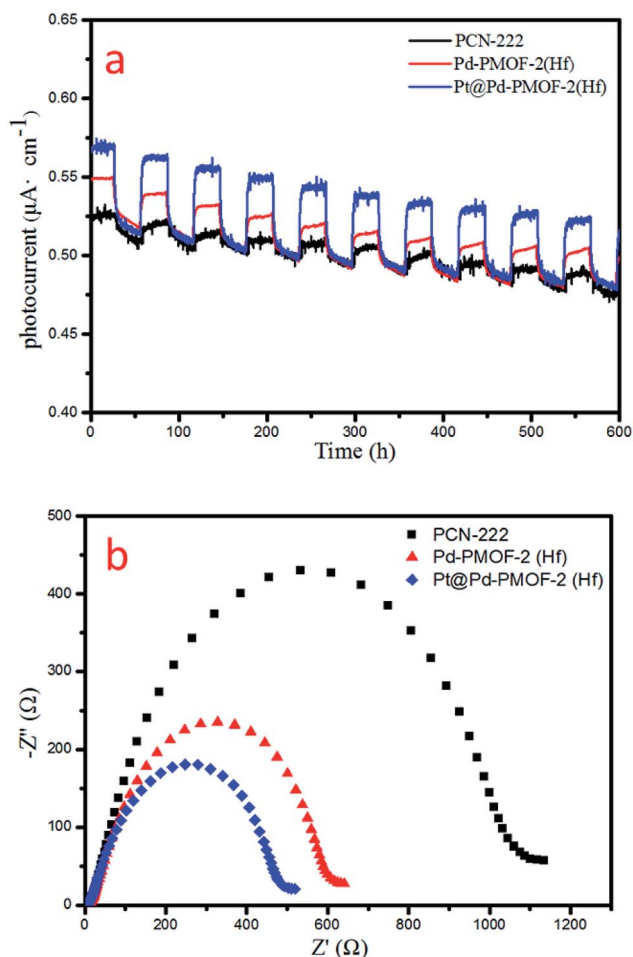


Fig. 8 Photocurrent responses (a) and EIS Nyquist plots (b) of PCN-222(Hf), Pd-PCN-222(Hf) and Pt@Pd-PCN-222(Hf).



water concentration effect that was enforced by hydrophilic Hf(IV)-oxo clusters. The developed MOF composite Pt@Pd-PCN-222(Hf) can avoid the aggregation of Pt-NPs, assist better electron transfer between Pd-porphyrin and Pt-NPs units, and promote the H<sub>2</sub> evolution rate. Further work on the design and catalytic applications of porphyrin-based MOFs is in progress.

## Conflicts of interest

There are no conflicts to declare.

## Acknowledgements

The authors acknowledge support from the National Natural Science Foundation of China (21773314, 21720102007, 21821003, and 21890380), Science and Technology Planning Project of Guangzhou (201707010168), and Local Innovative and Research Teams Project of Guangdong Pearl River Talents Program (2017BT01C161).

## Notes and references

- 1 A. J. Esswein and D. G. Nocera, *Chem. Rev.*, 2007, **107**, 4022–4047.
- 2 S. Y. Tee, K. Y. Win, W. S. Teo, L.-D. Koh, S. Liu, C. P. Teng and M.-Y. Han, *Adv. Sci.*, 2017, **4**, 1600337.
- 3 M. Reza Gholipour, C.-T. Dinh, F. Beland and T.-O. Do, *Nanoscale*, 2015, **7**, 8187–8208.
- 4 W. Wang, X. Xu, W. Zhou and Z. Shao, *Adv. Sci.*, 2017, **4**, 1600371.
- 5 K. Meyer, M. Ranocchiari and J. A. van Bokhoven, *Energy Environ. Sci.*, 2015, **8**, 1923–1937.
- 6 S. Wang and X. Wang, *Small*, 2015, **11**, 3097–3112.
- 7 M. Wen, K. Mori, Y. Kuwahara, T. An and H. Yamashita, *Appl. Catal., B*, 2017, **218**, 555–569.
- 8 B. Zhu, R. Zou and Q. Xu, *Adv. Energy Mater.*, 2018, **8**, 1801193.
- 9 J. Liu, L. Chen, H. Cui, J. Zhang, L. Zhang and C.-Y. Su, *Chem. Soc. Rev.*, 2014, **43**, 6011–6061.
- 10 C.-C. Cao, C.-X. Chen, Z.-W. Wei, Q.-F. Qiu, N.-X. Zhu, Y.-Y. Xiong, J.-J. Jiang, D. Wang and C.-Y. Su, *J. Am. Chem. Soc.*, 2019, **141**, 2589–2593.
- 11 C.-X. Chen, Z.-W. Wei, J.-J. Jiang, S.-P. Zheng, H.-P. Wang, Q.-F. Qiu, C.-C. Cao, D. Fenske and C.-Y. Su, *J. Am. Chem. Soc.*, 2017, **139**, 6034–6037.
- 12 Y. Zhang, J. Guo, L. Shi, Y. Zhu, K. Hou, Y. Zheng and Z. Tang, *Sci. Adv.*, 2017, **3**, e1701162.
- 13 Q. Lin, X. Bu, A. Kong, C. Mao, X. Zhao, F. Bu and P. Feng, *J. Am. Chem. Soc.*, 2015, **137**, 2235–2238.
- 14 M. H. Beyzavi, N. A. Vermeulen, A. J. Howarth, S. Tussupbayev, A. B. League, N. M. Schweitzer, J. R. Gallagher, A. E. Platero-Prats, N. Hafezi, A. A. Sarjeant, J. T. Miller, K. W. Chapman, J. F. Stoddart, C. J. Cramer, J. T. Hupp and O. K. Farha, *J. Am. Chem. Soc.*, 2015, **137**, 13624–13631.
- 15 Y.-Z. Chen, Z. U. Wang, H. Wang, J. Lu, S.-H. Yu and H.-L. Jiang, *J. Am. Chem. Soc.*, 2017, **139**, 2035–2044.
- 16 G. Lan, Y.-Y. Zhu, S. S. Veroneau, Z. Xu, D. Micheroni and W. Lin, *J. Am. Chem. Soc.*, 2018, **140**, 5326–5329.
- 17 X.-S. Wang, L. Meng, Q. Cheng, C. Kim, L. Wojtas, M. Chrzanowski, Y.-S. Chen, X. P. Zhang and S. Ma, *J. Am. Chem. Soc.*, 2011, **133**, 16322–16325.
- 18 A. Fateeva, P. A. Chater, C. P. Ireland, A. A. Tahir, Y. Z. Khimyak, P. V. Wiper, J. R. Darwent and M. J. Rosseinsky, *Angew. Chem., Int. Ed.*, 2012, **51**, 7440–7444.
- 19 J. Zheng, M. Wu, F. Jiang, W. Su and M. Hong, *Chem. Sci.*, 2015, **6**, 3466–3470.
- 20 Y. Zhao, N. Kornienko, Z. Liu, C. Zhu, S. Asahina, T.-R. Kuo, W. Bao, C. Xie, A. Hexemer, O. Terasaki, P. Yang and O. M. Yaghi, *J. Am. Chem. Soc.*, 2015, **137**, 2199–2202.
- 21 J. A. Johnson, B. M. Petersen, A. Kormos, E. Echeverria, Y.-S. Chen and J. Zhang, *J. Am. Chem. Soc.*, 2016, **138**, 10293–10298.
- 22 D. Feng, W.-C. Chung, Z. Wei, Z.-Y. Gu, H.-L. Jiang, Y.-P. Chen, D. J. Darensbourg and H.-C. Zhou, *J. Am. Chem. Soc.*, 2013, **135**, 17105–17110.
- 23 Y. Wang, H. Cui, Z.-W. Wei, H.-P. Wang, L. Zhang and C.-Y. Su, *Chem. Sci.*, 2017, **8**, 775–780.
- 24 J. Liu, Y.-Z. Fan, X. Li, Z. Wei, Y.-W. Xu, L. Zhang and C.-Y. Su, *Appl. Catal., B*, 2018, **231**, 173–181.
- 25 O. S. Finikova, A. V. Cheprakov and S. A. Vinogradov, *J. Org. Chem.*, 2005, **70**, 9562–9572.
- 26 L. Zang, H. Zhao, J. Hua, W. Cao, F. Qin, J. Yao, Y. Tian, Y. Zheng and Z. Zhang, *J. Mater. Chem. C*, 2016, **4**, 9581–9587.
- 27 C. Wang, K. E. deKrafft and W. Lin, *J. Am. Chem. Soc.*, 2012, **134**, 7211–7214.
- 28 D. Wang, Y. Song, J. Cai, L. Wu and Z. Li, *New J. Chem.*, 2016, **40**, 9170–9175.
- 29 J.-D. Xiao, Q. Shang, Y. Xiong, Q. Zhang, Y. Luo, S.-H. Yu and H.-L. Jiang, *Angew. Chem., Int. Ed.*, 2016, **55**, 9389–9393.
- 30 Y. Horiuchi, T. Toyao, M. Saito, K. Mochizuki, M. Iwata, H. Higashimura, M. Anpo and M. Matsuoka, *J. Phys. Chem. C*, 2012, **116**, 20848–20853.
- 31 X. Fang, Q. Shang, Y. Wang, L. Jiao, T. Yao, Y. Li, Q. Zhang, Y. Luo and H.-L. Jiang, *Adv. Mater.*, 2018, **30**, 1705112.
- 32 F. Leng, H. Liu, M. Ding, Q.-P. Lin and H.-L. Jiang, *ACS Catal.*, 2018, **8**, 4583–4590.
- 33 J. He, J. Wang, Y. Chen, J. Zhang, D. Duan, Y. Wang and Z. Yan, *Chem. Commun.*, 2014, **50**, 7063–7066.
- 34 M. Wen, K. Mori, T. Kamegawa and H. Yamashita, *Chem. Commun.*, 2014, **50**, 11645–11648.
- 35 J.-D. Xiao, L. Han, J. Luo, S.-H. Yu and H.-L. Jiang, *Angew. Chem., Int. Ed.*, 2018, **57**, 1103–1107.
- 36 J. He, Z. Yan, J. Wang, J. Xie, L. Jiang, Y. Shi, F. Yuan, F. Yu and Y. Sun, *Chem. Commun.*, 2013, **49**, 6761–6763.
- 37 J. Guo, Y. Zhang, L. Shi, Y. Zhu, M. F. Mideksa, K. Hou, W. Zhao, D. Wang, M. Zhao, X. Zhang, J. Lv, J. Zhang, X. Wang and Z. Tang, *J. Am. Chem. Soc.*, 2017, **139**, 17964–17972.
- 38 J. H. Cavka, S. Jakobsen, U. Olsbye, N. Guillou, C. Lamberti, S. Bordiga and K. P. Lillerud, *J. Am. Chem. Soc.*, 2008, **130**, 13850–13851.





- 39 V. Guillermin, F. Ragon, M. Dan-Hardi, T. Devic, M. Vishnuvarthan, B. Campo, A. Vimont, G. Clet, Q. Yang, G. Maurin, G. Ferey, A. Vittadini, S. Gross and C. Serre, *Angew. Chem., Int. Ed.*, 2012, **51**, 9267–9271.
- 40 D. Feng, Z.-Y. Gu, J.-R. Li, H.-L. Jiang, Z. Wei and H.-C. Zhou, *Angew. Chem., Int. Ed.*, 2012, **51**, 10307–10310.
- 41 W. Morris, B. Voloskiy, S. Demir, F. Gandara, P. L. McGrier, H. Furukawa, D. Cascio, J. F. Stoddart and O. M. Yaghi, *Inorg. Chem.*, 2012, **51**, 6443–6445.
- 42 Y. Chen, T. Hoang and S. Ma, *Inorg. Chem.*, 2012, **51**, 12600–12602.
- 43 J. Canivet, A. Fateeva, Y. Guo, B. Coasne and D. Farrusseng, *Chem. Soc. Rev.*, 2014, **43**, 5594–5617.
- 44 J.-P. Zhang, A.-X. Zhu, R.-B. Lin, X.-L. Qi and X.-M. Chen, *Adv. Mater.*, 2011, **23**, 1268–1271.
- 45 M. Sadakiyo, T. Yamada and H. Kitagawa, *J. Am. Chem. Soc.*, 2011, **133**, 11050–11053.
- 46 R. Fareghi-Alamdari, M. Golestanzadeh and O. Bagheri, *RSC Adv.*, 2016, **6**, 108755–108767.
- 47 Y.-Z. Chen and H.-L. Jiang, *Chem. Mater.*, 2016, **28**, 6698–6704.
- 48 F. Su, C. K. Poh, Z. Tian, G. Xu, G. Koh, Z. Wang, Z. Liu and J. Lin, *Energy Fuels*, 2010, **24**, 3727–3732.
- 49 P. Falcaro, R. Ricco, A. Yazdi, I. Imaz, S. Furukawa, D. Maspoth, R. Ameloot, J. D. Evans and C. J. Doonan, *Coord. Chem. Rev.*, 2016, **307**, 237–254.
- 50 Q. Yang, Q. Xu and H.-L. Jiang, *Chem. Soc. Rev.*, 2017, **46**, 4774–4808.
- 51 C. Gomes Silva, I. Luz, F. X. Llabrés i Xamena, A. Corma and H. García, *Chem.–Eur. J.*, 2010, **16**, 11133–11138.
- 52 H.-Q. Xu, J. Hu, D. Wang, Z. Li, Q. Zhang, Y. Luo, S.-H. Yu and H.-L. Jiang, *J. Am. Chem. Soc.*, 2015, **137**, 13440–13443.
- 53 J.-D. Xiao, Q. Shang, Y. Xiong, Q. Zhang, Y. Luo, S.-H. Yu and H.-L. Jiang, *Angew. Chem., Int. Ed.*, 2016, **55**, 9389–9393.
- 54 X. Fang, Q. Shang, Y. Wang, L. Jiao, T. Yao, Y. Li, Q. Zhang, Y. Luo and H.-L. Jiang, *Adv. Mater.*, 2018, **30**, 1705112.
- 55 Z.-C. Kong, J.-F. Liao, Y.-J. Dong, Y.-F. Xu, H.-Y. Chen, D.-B. Kuang and C.-Y. Su, *ACS Energy Lett.*, 2018, **3**, 2656–2662.
- 56 A. Antipas and M. Gouterman, *J. Am. Chem. Soc.*, 1983, **105**, 4896–4901.

